

pubs.acs.org/JPCB Article

# Experimental Depth Profiles of Surfactants, Ions, and Solvent at the Angstrom Scale: Studies of Cationic and Anionic Surfactants and Their Salting Out

Published as part of The Journal of Physical Chemistry virtual special issue "Peter J. Rossky Festschrift".

Xianyuan Zhao,\* Gilbert M. Nathanson,\* and Gunther G. Andersson\*



Cite This: J. Phys. Chem. B 2020, 124, 2218-2229



**Read Online** 

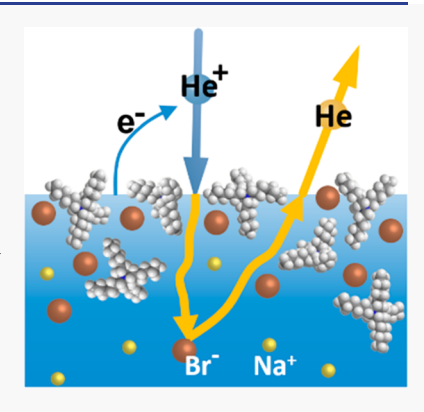
**ACCESS** 

Metrics & More

Article Recommendations

Supporting Information

**ABSTRACT:** Neutral impact ion scattering spectroscopy (NICISS) is used to measure the depth profiles of ionic surfactants, counterions, and solvent molecules on the angstrom scale. The chosen surfactants are  $0.010 \, m$  tetrahexylammonium bromide (THA<sup>+</sup>/Br<sup>-</sup>) and  $0.0050 \, m$  sodium dodecyl sulfate (Na<sup>+</sup>/DS<sup>-</sup>) in the absence and presence of  $0.30 \, m$  NaBr in liquid glycerol. NICISS determines the depth profiles of the elements C, O, Na, S, and Br through the loss in energy of 5 keV He atoms that travel into and out of the liquid, which is then converted into depth. In the absence of NaBr, we find that THA<sup>+</sup> and its Br<sup>-</sup> counterion segregate together because of charge attraction, forming a narrow double layer that is  $10 \, \text{Å}$  wide and  $150 \, \text{times}$  more concentrated than in the bulk. With the addition of NaBr, THA<sup>+</sup> is "salted out" to the surface, increasing the interfacial Br<sup>-</sup> concentration by 3-fold and spreading the anions over a  $\sim 30 \, \text{Å}$  depth. Added NaBr similarly increases the interfacial concentration of DS<sup>-</sup> ions and broadens their positions. Conversely, the dissolved Br<sup>-</sup> ions are significantly depleted over a depth of  $0-40 \, \text{Å}$  from the surface because of charge repulsion from DS<sup>-</sup> ions within the interfacial region. These different interfacial Br<sup>-</sup>



propensities correlate with previously measured gas—liquid reactivities: gaseous Cl<sub>2</sub> readily reacts with Br<sup>-</sup> ions in the presence of THA<sup>+</sup> but drops 70-fold in the presence of DS<sup>-</sup>, demonstrating that surfactant headgroup charge controls the reactivity of Br<sup>-</sup> through changes in its depth profile.

### ■ INTRODUCTION

Soluble ionic surfactants are often composed of a charged organic group and an oppositely charged inorganic counterion. Two prominent examples are alkylammonium cations paired with halide anions and alkyl sulfate anions paired with alkali metal cations. These ionic compounds display a remarkable property when dissolved in water: the surface-active organic ions segregate to the surface, dragging with them their nominally surface inactive inorganic counterions. This interfacial enrichment in inorganic ions is expected on the basis of local charge attraction between the two ions, and it has been confirmed by experiments and simulations. 1-6 We ask in this study how both surfactant and inorganic ions distribute themselves in the interfacial region on the angstrom scale and how these depth distributions are altered when the surfactant ion pair is "salted out" toward the interfacial region by addition of an alkali halide. 7,8 The chosen systems are the cationic surfactant tetrahexylammonium bromide (THA+/Br-) and the anionic surfactant sodium dodecyl sulfate (Na+/DS-) in the absence and presence of Na<sup>+</sup>/Br<sup>-</sup> salt in liquid glycerol (Figure 1a).

Historically, the primary tool for investigating surface enrichment of soluble ionic surfactants is the decrease in surface tension upon adding solute and its analysis via the Gibbs adsorption equation. 8-11 This powerful method reveals how organic—inorganic ion pairs generate a positive or negative relative surface excess, equal to their concentrations integrated over the depth of the inhomogeneous interfacial region with respect to their bulk-phase concentrations. Surface tension measurements do not, however, yield the surfactant and counterion concentrations as a function of depth. Such depth profiles on the atomic scale can be explored by X-ray photoelectron spectroscopy, 1,12-14 neutron and X-ray reflectivity, 15-19 ion scattering spectroscopies, 20 sum-frequency generation, 21 and molecular simulations. 3,9,14,22,23 The technique applied here, neutral impact-collision ion scattering spectroscopy (NICISS), enables measurements of elemental depth profiles beyond 100 Å with an uncertainty (in the compression or extension of the depth axis) of less than ±20%. 20,24,25 It has also been used to roughly resolve the nonmonotonic iodide

Received: December 18, 2019
Revised: February 14, 2020
Published: February 19, 2020



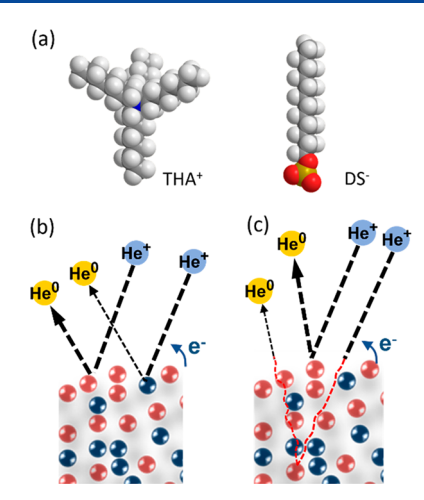


**Figure 1.** (a) Space-filling pictures of tetrahexylammonium (THA<sup>+</sup>) and dodecyl sulfate (DS<sup>-</sup>). (b) Illustration of NICISS (neutral impact collision ion scattering spectroscopy). He<sup>+</sup> ions strike a mixture of light (blue) and heavy (red) atoms and are neutralized upon impact. Left side: He atoms transfer more energy to lighter atoms and scatter backward at lower speeds than when they collide with heavier atoms. Right side: most He atoms penetrate between the top surface molecules and undergo grazing collisions (small angle scattering) with molecules deeper in the liquid. This extra energy loss can be correlated with atom depth in solution.

distribution in a LiI/formamide solution over 15 Å, as predicted by molecular dynamics simulations for alkali bromide and iodide solutions in formamide <sup>26</sup> and in water. <sup>9,27–30</sup> Such oscillations have also been reported for Er³+ in ErCl₃ (aq) by X-ray reflectivity. <sup>18</sup> Most pertinent to this study, NICISS has revealed the concentration depth profiles for numerous surfactants and their counterions. <sup>5,20,31–33</sup> Because NICISS relies on collisions of He⁺ ions with liquids in vacuum, it has mostly been applied to low vapor pressure solvents such as formamide and glycerol. This limitation is not essential: by carefully subtracting collisions in the vapor, NICISS has been used to map the enrichment of I⁻ in a solution of tetrabutylammonium iodide and LiCl in water at 260 K. <sup>34</sup> However, measurements with high vapor pressure solvents such as water require additional calibration procedures that make the measurements more complicated. <sup>34,35</sup>

The NICISS technique is illustrated in Figure 1b, which depicts collisions of He<sup>+</sup> ions with a liquid mixture of light and heavy species. These incoming ions are almost completely neutralized by electron transfer from solute or solvent molecules upon impact at the surface. The resulting He atoms either backscatter directly from the outermost atoms of the solvent or continue moving into solution. The final kinetic energy of the He atom depends on the mass of the target atom (the atom from which the He projectile backscatters): He atoms lose less energy when the surface atom is heavier and more energy when the atom is lighter. Thus, the backscattered He atoms report on the mass and identity of these surface atoms.

Importantly, most high-energy He atoms pass between the surface and subsurface atoms (Figure 1c) through grazing angle collisions, losing a small fraction of their energy (a few electronvolts per collision) as they penetrate into solution. He atoms that collide head-on with an atom deeper in the liquid will bounce backward and again undergo grazing collisions before emerging into the vacuum. The energy loss per Angstrom through small angle scattering (called the "stopping power") is calibrated using alkanethiol monolayers of known variable

thickness and is used to convert the measured He backscattering energy into depth of the target atom.  $^{36}$  This analysis is carried out in detail in the Supporting Information. Additional model calculations predict that this energy loss increases by  $\sim 15\%$  when the hydrocarbon chains are replaced by liquid glycerol.  $^{37,38}$  We emphasize that NICISS is sensitive only to the identity of individual atoms and not to their charge state or the structure of the molecule.

We also remark that the NICISS depth distributions are not broadened by the undulating interfacial step heights generated by thermal roughening (capillary wave broadening). This is because zero depth starts when the He atom collides with the outermost atom, regardless of this atom's position with respect to neighboring atoms, and because the He atoms travel fast enough that they only sample a static distribution. In this sense, the depth profiles produced by NICISS should share features with the instantaneous or intrinsic interfacial profiles calculated theoretically, <sup>28,40</sup> but averaged over the experimental uncertainty.

We chose glycerol, HOCH $_2$ CH (OH)CH $_2$ OH, for these studies because it is a low vapor pressure ( $10^{-4}$  Torr), protic liquid with a high dielectric constant of 44 in which salts such as NaBr dissolve substantially (at least 3 M in glycerol versus 9 M in water). It differs chiefly from water in its large viscosity (1200 cP versus 1 cP in water) due to extensive hydrogen bonding. The surface tension of glycerol of 63 mN m $^{-1}$  is just slightly lower than the 72 mN m $^{-1}$  value for water, although SFG measurements and simulations show that the dangling hydrogen bonds at the surface of water are all capped at the surface of glycerol.

The NICISS experiments were originally motivated to interpret reactive scattering studies involving collisions of gaseous Cl<sub>2</sub> with dissolved 0.3 m Br<sup>-</sup> ions in liquid glycerol via the reaction  $Cl_2(g) + 2Br^- \rightarrow Br_2(g) + 2Cl^{-44}$  The addition of just 0.01 m THA<sup>+</sup>/Br<sup>-</sup> was found to enhance production of Br<sub>2</sub> by 14-fold, while the substitution of 0.005 m Na $^+$ /DS $^$ suppressed reactivity by 5-fold. Each surfactant is pictured in Figure 1a: THA<sup>+</sup> is composed of four hexyl chains tethered to a central N atom, while DS links a single dodecyl chain to a sulfate headgroup. The remarkable ability of these surfactants to control interfacial reactions of Br by 70-fold are reflected in the concentrations measured by NICISS in this study. The experiments reveal significant changes in the depth distributions of THA+, DS-, and Br- upon addition of NaBr. In particular, they show that dense surfactant and counterion layers form close to the outermost surface, followed by a more dilute region that extends up to 70 Å into solution. These distributions provide a microscopic picture of the "salting out" of the two surfactants to the surface by added NaBr, and especially of the propensity of Br to be enriched near the surface by cationic surfactants and repelled by anionic ones. The depth profiles further show how enhanced solute concentrations are balanced by significant depletion of the glycerol solvent itself, creating an interfacial region rich in alkyl chains and inorganic ions.

# **EXPERIMENTAL METHODS**

The NICISS apparatus, pictured in Figure 2, consists of three regions with different functions: He<sup>+</sup> ion generation, production of continuously renewed liquid films, and time-of-flight (TOF) detection of the backscattered neutral He atoms. Each component is described briefly below.<sup>24</sup>

Ion Beam Generation and Time-of-flight Detection. A continuous 5000 eV helium ion beam was produced by electron

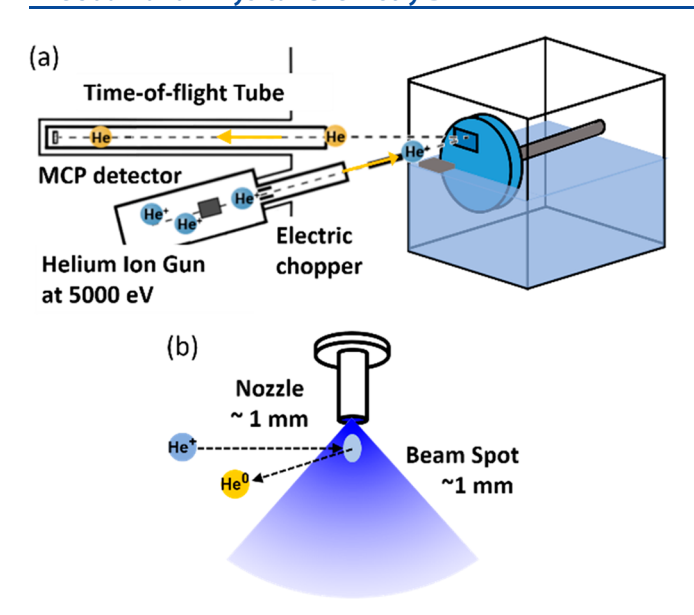


**Figure 2.** NICISS apparatus. (a) 5000 eV He<sup>+</sup> ions strike the surface of a surfactant-salt-glycerol solution that coats a rotating wheel. A fraction of the neutralized He atoms scatter at a deflection angle of 165° and are detected by a microchannel plate within a 0.3 ns time window. (b) Gasphase spectra are measured over a 1 mm diameter spot from gas emanating from a 1 mm hole.

impact of the He gas. Ion pulses were then created by electric deflection at a frequency of 100 kHz with a pulse width of less than 10 ns (duty cycle <0.1%), resulting in a current of 0.2 nA. This chopped He<sup>+</sup> beam was directed at the liquid sample located 35.0 cm from the deflector, projecting a 1 mm diameter spot on the surface. Neutralized He atoms were collected at a backscattering angle of 165° in order to minimize the signal from multiple medium-angle collisions. After traveling 135.0 cm in a time-of-flight (TOF) tube, the He atoms were detected by a chevron microchannel plate with typically close to 100% detection at He backscattering energies greater than 1000 eV.

Liquids and Rotating Coated Wheel Assembly. NaBr, THABr, and SDS were purchased from Sigma-Aldrich (purity >99%) and used without further purification. Salty glycerol solutions were prepared by dissolving a surfactant into pure glycerol or 0.3 m NaBr with mild heating (<313 K) and stirring under vacuum to accelerate surfactant dissolution and remove dissolved gas and water. 46 After degassing, the liquid was transferred to a stainless-steel reservoir as shown in Figure 2a and then loaded into the vacuum chamber. A rotating stainlesssteel wheel 30 mm in diameter was half-immersed in solution to produce a continuously renewed, < 0.3 mm thick liquid film after passing by a stainless-steel scraper. The time from scraping to ion beam exposure was set to 3 s for most experiments, which also corresponds to the time for the dissolved surfactant to segregate to the surface. Experiments using THABr + NaBr at two rotations speeds corresponding to film formation times of 1 and 3 s revealed identical He TOF spectra, indicating that 3 s is sufficient for bulk-phase THA+/Br- to reach the surface. 47 The He<sup>+</sup> flux was low enough that fewer than 0.01% of the surface molecules were exposed to He<sup>+</sup> ions as the film rotates through the ion beam. In all experiments, a cooling panel attached to the reservoir maintained the temperature at 293 K. The scattering chamber was kept below  $2 \times 10^{-5}$  mbar during experiments using a liquid nitrogen trap and a 550 L s<sup>-1</sup> turbomolecular pump.

Gas-Phase Calibration Experiments. Bromoform, thiophene, and air were used for determining the backscattering energy loss from isolated bromine, sulfur, and oxygen atoms, respectively. 48 Gas-phase samples were introduced through a 1 mm diameter pinhole located 1 mm above the scattering region, as shown in Figure 2b. Example spectra can be found later in Figures 4 and 10 for Br and S. Three factors contribute to the tens of electron volt width of the gas-phase spectra: the  $\sim$ 1 mm spatial dimension of the gas beam, the 10 ns width in time of the ion gas pulse, and most importantly, energy transfer from the high-energy He atom to numerous excitations of core electrons of the target atom. <sup>20</sup> The resulting gas-phase spectra are then modeled by Gaussian distributions, which are used to deconvolute the observed liquid-phase spectra presented below. In particular, we estimate an uncertainty of  $\pm 1.5$  Å in the assignment of zero depth for Br ions, which arises from a ±12 eV uncertainty in the peak energy of the gas-phase CHBr<sub>3</sub> spectrum.

Molar Concentration Calculations. The elemental concentrations c(z) as a function of depth z are calculated from the He backscattering signal S(z), after converting from the arrival time in the TOF spectrum to He kinetic energy to liquid depth, as outlined in refs 24 and 31 and in the Supporting Information. The conversion from a relative to absolute concentration on a molarity scale is accomplished by noting that  $S(z) = c(z) \cdot d\sigma(z) / d\omega \cdot a$ , where  $d\sigma(z) / d\omega$  is the normalized differential He-target collision cross section into the 165° backscattering direction, and a is a machine-dependent sensitivity factor. Absolute concentrations are obtained by scaling the signal at z to the signal at large depths near 70 Å where the bulk concentration is known. In all solutions investigated here, the glycerol oxygen atoms deep in the bulk generate the strongest NICISS signal. This signal is used as a reference, correlated with an O atom concentration of  $c_0$  (bulk) = 41 M =  $3 \cdot [glycerol molarity of 13.7 M]$ . The resulting expression for the Br<sup>-</sup> depth profile is<sup>49</sup>

$$c_{\rm Br}(z) = \frac{S_{\rm Br}(z)}{S_{\rm oxy}({\rm bulk})} \frac{({\rm d}\sigma({\rm bulk})/{\rm d}\omega)_{\rm oxy}}{({\rm d}\sigma(z)/{\rm d}\omega)_{\rm Br}} c_{\rm oxy}({\rm bulk}) \tag{1}$$

Analogous equations are used to determine the O, C, S, and Na<sup>+</sup> molar depth profiles.

**Electrical Neutrality.** The requirement of equal numbers of cations and anions in the interfacial region is a strict test of the NICISS technique.<sup>31</sup> Appendix I shows that the THA<sup>+</sup>, Na<sup>+</sup>, Br<sup>-</sup>, and DS<sup>-</sup> concentrations extracted from the TOF spectra satisfy charge balance within 5–22%.

# ■ RESULTS, ANALYSIS, AND DISCUSSION

We prepared six glycerol solutions, including four containing Br<sup>-</sup> ions. In each case, our objective is to measure and interpret the Br<sup>-</sup>, surfactant ion, and glycerol depth profiles. These solutions are (1) pure glycerol, (2) added salt 0.30 molal (0.38 Molar) NaBr, (3) added cationic surfactant 0.010 m (0.013 M) THABr, (4) added cationic surfactant + salt 0.010 m THABr + 0.30 m NaBr (0.013 M THABr + 0.38 M NaBr), (5) added anionic surfactant 0.0050 m (0.0064 M) SDS, and (6) added anionic surfactant + salt 0.0050 m SDS + 0.30 m NaBr (0.0064 M SDS + 0.38 M NaBr).

**Photon Emission and Zero Arrival Time.** The TOF spectrum of He atoms backscattering from the THABr + NaBr solution is shown in Figure 3 in order to demonstrate its key features. The leftmost peak is produced by photon emission

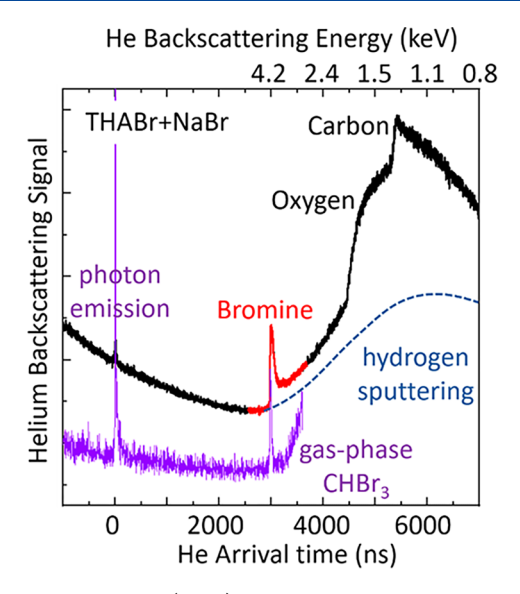


**Figure 3.** Time-of-flight (TOF) spectrum of He atoms backscattering from a  $0.01 \, m$  THABr +  $0.3 \, m$  NaBr glycerol solution. The Br, O, and C elements are labeled, along with the photon emitted as He $^+$  is neutralized. The red color highlights He atoms scattering from Br $^-$  ions at positions at the surface (sharp peak) and below the surface (longer arrival times). The CHBr $_3$  gas-phase spectrum (purple) overlaps in arrival time with the liquid-phase photon and Br peaks.

upon He<sup>+</sup> impact at the surface. <sup>50</sup> Because the photon is emitted at the instant that He<sup>+</sup> reaches the surface, its arrival at the detector serves as a time stamp of the He backscattering collision. This photon arrives 4.5 ns after traveling the 1.35 m flight distance, and therefore time zero in the TOF spectrum is shifted by this time before the center of photon peak.

**Identifying Individual Atoms in Solution.** All of the features related to surface composition and structure are found after 2000 ns in Figure 3. These signals correspond to He atoms backscattered from atoms in the liquid over a depth of  $\sim 100$  Å. Helium atoms backscatter from heavier elements with less energy loss and therefore higher velocities and shorter arrival times. These arrival times can be gauged by the kinematics of elastic collisions:

$$\frac{E}{E_0} = \left(\frac{\cos\theta + \sqrt{A^2 - \sin^2\theta}}{1 + A}\right)^2 \tag{2}$$

where E is the backscattered energy of the He atom,  $E_0 = 5000$  eV is the He primary beam energy,  $\theta = 165^\circ$  is the angle of deflection, and  $A = m_{\rm target}/m_{\rm He}$  is the mass ratio of target and He atoms. As an example, a 5.0 keV He atom will retain 4.1 keV after backscattering from a Br $^-$  ion, the heaviest element in the THABr + NaBr solution. This signal appears at 3000 ns in the TOF spectrum. Each feature in the spectrum is attributed to an element by aligning the onset of the signal with the kinematic prediction, which typically match within 100 ns. For the THABr + NaBr spectrum in Figure 3, we can identify Br, O, and C, while N and Na are too weak to be observed.

Fine Structure: Surface versus Subsurface Br<sup>-</sup> Atoms. The spread in arrival times of He atoms backscattering from each element reflects their depths in solution. As shown in Figure 3, the sharp gas-phase CHBr<sub>3</sub> peak at 3000 ns, which corresponds to single backward collisions between He and Br, overlaps well with the onset of the solution-phase Br peak. This signal corresponds to He atoms backscattering from Br<sup>-</sup> ions in

the outermost surface layer without any intervening atoms that would cause extra energy loss through grazing collisions. This high-energy onset is therefore assigned to zero depth at the start of the liquid phase. The signal at longer arrival times (greater energy loss) in the region of the Br peak corresponds to He atoms that scatter from subsurface O and C atoms of glycerol and THA<sup>+</sup>, strike a deeper Br<sup>-</sup> ion head-on, and then emerge at the 165° backscattering angle of the detector. We will analyze this lower energy component of the spectrum below in order to determine the Br<sup>-</sup> depth profile. We note that the Br signal appears as a sharp peak because it is the counterion to THA<sup>+</sup>, which segregates to a narrow surface region and drags Br<sup>-</sup> with it to maintain charge neutrality.

The O and C assignments in Figure 3 will also be analyzed later in terms of contributions from glycerol and THA<sup>+</sup>. Highenergy He atoms do not backscatter from H atoms, which are less massive than He, but some H atoms in the collision zone are sputtered from molecules near the surface and broadly scatter over a range of speeds and energies. These high-energy H atoms trigger the detector and form the rising background in Figure 3. As described in ref 11, this background is subtracted by fitting it to a smooth polynomial.

Qualitative Analysis of Br Ion Interfacial Depth Profiles. Figure 4 collects the He TOF spectra from all

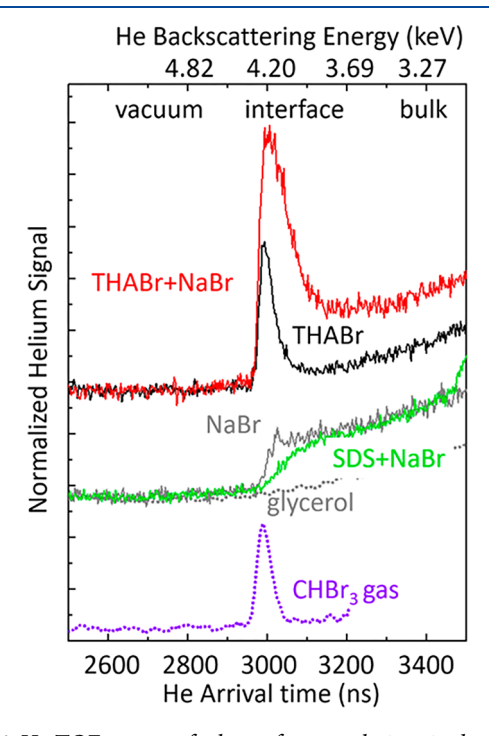


**Figure 4.** He TOF spectra of salt—surfactant solutions in the region of  $\mathrm{Br}^-$  detection: 0.01 m THABr + 0.3 m NaBr (red), 0.01 m THABr (black), pure 0.3 m NaBr (gray), and 0.005 m SDS + 0.3 m NaBr (green). The gas-phase spectra for He backscattered from gas-phase CHBr $_3$  (purple) and from pure glycerol (dotted) are shown for comparison. The solution spectra are normalized to the constant glycerol O atom signal at large depths.

solutions in the 3000 ns neighborhood of He atoms back-scattering from Br<sup>-</sup> ions. The six spectra span pure glycerol and solutions of NaBr, THABr, THABr + NaBr, and SDS + NaBr, along with gas-phase CHBr<sub>3</sub>. Several features stand out. Both THABr solutions generate a sharp Br<sup>-</sup> peak, reflecting the segregation of Br<sup>-</sup> to a narrow interfacial region as the

counterion of the THA<sup>+</sup> surfactant. It is evident that the Br<sup>-</sup> signal increases substantially when NaBr is added to THABr, implying that NaBr "salts out" THA<sup>+</sup> cations and pushes them toward the surface, dragging even more Br<sup>-</sup> anions with them. The Br<sup>-</sup> signal for NaBr/glycerol appears just as a step function with a sloping edge, indicating that Br<sup>-</sup> ions are present in the interfacial region but do not preferentially collect there in the absence of a surfactant. In sharp contrast, the Br<sup>-</sup> signal from the SDS + NaBr solution is depleted in the interfacial region because of charge repulsion between the Br<sup>-</sup> and surface dodecyl sulfate (DS<sup>-</sup>) anions. Pure glycerol lacks any atoms with the mass of Br and is flat in this region. As mentioned above, the sloping shape of the Br signal from pure NaBr/glycerol does not arise from thermal broadening of the interfacial region but instead reflects the finite spatial resolution of the experiments.

Deconvolution of the He TOF Spectra and Quantitative Depth Profiles for Br in TBABr. The He TOF spectra are convolutions of the true distributions of He atom energy losses and the experimental broadening factors discussed above that are present in the gas-phase spectra as well. We use a genetic algorithm to carry out the deconvolution because it does not assume a predetermined shape for the depth profile, as described in refs 31 and 48. On the basis of experiments measuring the penetration of He atoms into alkanethiolate monolayers,<sup>3</sup> deduce an energy loss of  $4.0 \pm 0.7$  eV Å<sup>-1</sup> for 5000 eV He atoms, which becomes smaller as the He atom loses energy through small angle scattering. We assume that this energy loss applies to both oxygen and carbon atoms of the solvent and surfactants, while less frequent grazing collisions with Br<sup>-</sup>, Na<sup>+</sup>, and S atoms are ignored in this analysis (where Br accounts for 1 in 26 heavy atoms in THABr and Na<sup>+</sup> and S accounts for 1 in 17 heavy atoms in SDS). The effect of the  $\pm 0.7$  eV Å<sup>-1</sup> uncertainty is to expand or compress the depth scale by 17% for each spectrum while leaving all comparisons unchanged. See the Supporting Information for a detailed procedure to convert He atom arrival time to depth of the target atom.

Figure 5 illustrates the effect of deconvoluting the spread in He energies measured for gas-phase CHBr<sub>3</sub> from the spread in energies of He backscattering from Br<sup>-</sup> ions in the 0.013 M THABr solution. The two depth profiles are plots of Br<sup>-</sup> concentration in molar units versus depth in Angstroms. The raw, undeconvoluted curve in Figure 5 is just the TOF spectrum in arrival time converted to backscattering energy according to  $E = \frac{1}{2} m_{\rm He} (L/t)^2$  and then converted from energy to depth. The spillover at negative depths is due to the finite energy resolution of the experiment. In contrast, the deconvoluted spectrum is forced to zero concentration at zero depth because Br<sup>-</sup> ions do not exist in vacuum.

The deconvoluted Br $^-$  depth profile in Figure 5 indicates that the full-width at half-maximum (fwhm) is  $10 \pm 2$  Å, which roughly corresponds to the size of two glycerol molecules or one THA $^+$  ion. This spread is the range of Br $^-$  ion depths due to their attraction to surface THA $^+$  ions at 283 K. Similarly narrow widths starting at zero depth have been observed in prior studies of tetrabutylammonium and phosphonium salts in formamide.  $^{5,31,51}$  The error bars represent  $\pm$  one standard deviation of 10000 trial profiles generated by the genetic algorithm. Their large size arises from the sharpness of the Br $^-$  peak (shown in Figure 4), which is nearly the same width as the gas-phase Br signal from CHBr $_3$  used for deconvolution. The maximum Br $^-$  concentration is near 2 M, or  $\sim$ 150 times larger than the 0.013 M bulk THABr concentration. We note that any curve drawn between the error bars that preserves the overall area of the

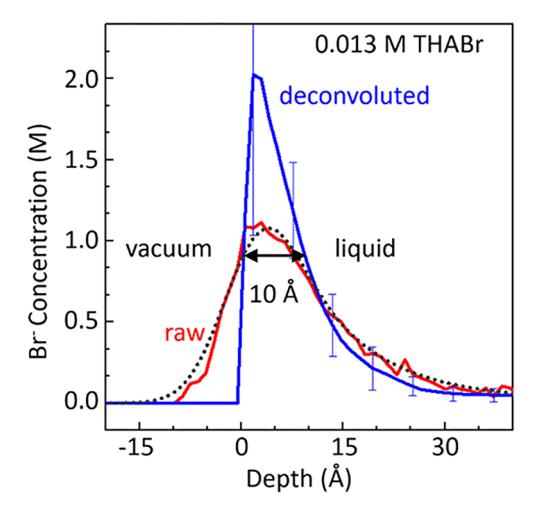


**Figure 5.** Raw (red) and deconvoluted (blue) depth profiles of Br<sup>-</sup> in the 0.013 M (0.010 m) THABr/glycerol solution. The blue curve is calculated by the genetic algorithm, which generates error bars that represent  $\pm$  one standard deviation of 10000 trial fits. The 2 M peak Br $^{-}$  concentration of is 150 times greater than the 0.013 M bulk THABr concentration. The dotted curve tests the reliability of the genetic algorithm: it is the convolution of the blue curve with the experimental broadening factors used in the original deconvolution.

distribution is a possible depth profile. The blue curve in Figure 5 is the average of all trials and represents the best overall fit. As shown by the dashed line, the convolution of this best fit with the gas-phase Br profile matches well with the raw profile. This overlap reflects the ability of the genetic algorithm to generate depth profiles that reproduce the original data.

The ~10 Å width of the Br<sup>-</sup> depth profile in Figure 5 must reflect the charge and dispersion attractions between the THA<sup>+</sup> and Br<sup>-</sup> ions, their solvation by glycerol, and their thermal motions. Perhaps the simplest prediction comes from the Bjerrum critical distance, which balances charge attraction and thermal energy in a solvent of dielectric constant  $\varepsilon_{\rm r}$ . This balancing leads to a minimum in the number of ions in a shell around the central ion at a separation distance  $d={\rm e}^2/(2\varepsilon_{\rm r}k_{\rm B}T)\approx$  7 Å using  $\varepsilon_{\rm r}=44$  for pure glycerol at 293 K, which can be considered the maximum separation for THA<sup>+</sup>/Br<sup>-</sup> ion pairing. Such a continuum prediction for isolated ions may not apply in the interfacial region, where alkyl chains, ion charges, and glycerol solvent are closely packed, but it appears to roughly gauge the fluctuating distribution of Br<sup>-</sup> ions tethered to THA<sup>+</sup> in Figure 5.

Surfactant Salting-Out Interpreted through Br Depth **Profiles.** Figure 6 compares the deconvoluted depth profiles of Br for pure THABr, pure NaBr, THABr + NaBr, and SDS + NaBr. They confirm the qualitative description above and provide an angstrom-scale picture of what charge attraction and repulsion and salting-out look like for the Br ion. Perhaps the most striking feature is that the addition of NaBr to THABr significantly increases the number and spread of Br ions, extending the fwhm of the depth profiles from 10 to 30 Å. This  $30 \pm 6$  Å width is equal to the size of  $\sim 3$  THA<sup>+</sup> ions or six glycerol molecules, thus penetrating far beyond the top surface layer. As shown later in Figure 10, this width is roughly matched by the distribution of THA<sup>+</sup> itself, suggesting tight Br<sup>-</sup>/THA<sup>+</sup> ion pairing persists below the surface as well. We do not know whether the shoulder at 35 Å is statistically meaningful, as it is possible to draw a smooth curve within the error bars.

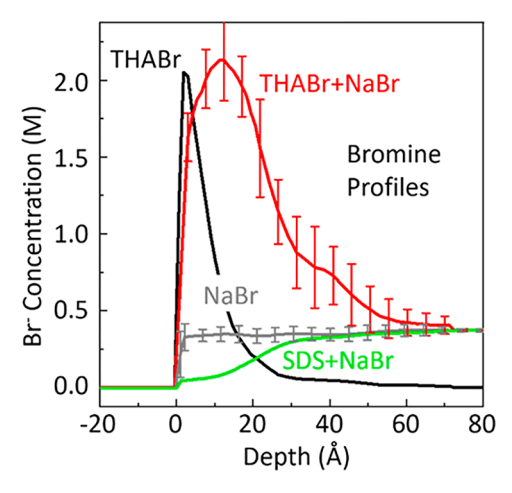
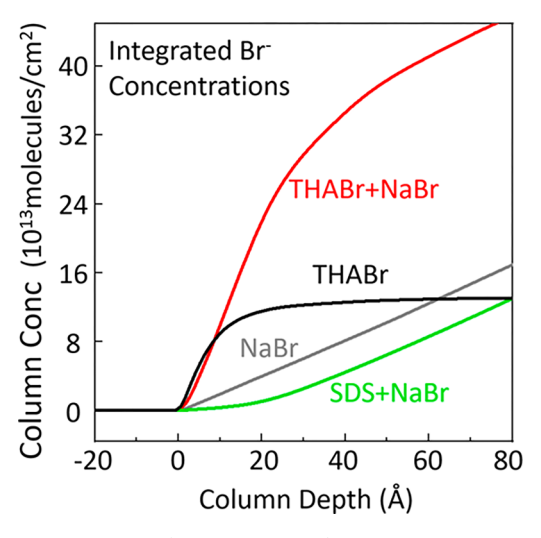


Figure 6. Deconvoluted depth profiles for  $Br^-$  ions in 0.013 M THABr (black), 0.013 M THABr + 0.38 M NaBr (red), 0.38 M NaBr (gray), and 0.0064 M SDS + 0.38 M NaBr (green). The addition of THABr to NaBr (gray  $\rightarrow$  red profiles) attracts significant  $Br^-$  ions to the surface region, while the addition of SDS to NaBr (gray  $\rightarrow$  green profiles) repels  $Br^-$  into the bulk.

Figure 6 also reveals that the peak Br<sup>-</sup> concentration does not rise significantly from its 2 M value in THABr alone. This surprising result may arise because the surface of 0.013 M THABr is already so packed with THA<sup>+</sup> and Br<sup>-</sup> ions that it is more favorable for additional ions to collect below the outermost layers than to squeeze into the outermost layer. Using an additive (McGowan) volume of ~650 Å<sup>3</sup> for THA<sup>+</sup>/Br<sup>-</sup> from refs 53 and 54, the maximum possible concentration is 2.6 M (devoid of solvent), a value that is just 30% larger than the deconvoluted 2 M peak concentration in Figure 6. In this picture, most "salted out" Br<sup>-</sup> ions are not driven to occupy only empty surface sites but instead span positions up to 60 Å deep.

Finally, Figure 6 also highlights the severe depletion of Brions in the presence of dodecyl sulfate ions of the same charge, with a midway point of  $\sim$ 20 Å. This depleted region extends over the distribution of sulfate headgroups (shown later in Figure 13), which also penetrate deeply into glycerol. The pure NaBr solution shows neither segregation nor depletion, but a sharp drop near zero depth. As mentioned in the Introduction, we do not have high enough resolution to judge whether a nonmonotonic Br $^-$  density profile exists within the top few monolayers of solution.

These analyses are summarized by plotting the integrated Br<sup>-</sup> concentration  $c_{Br}(z)$  as a function of depth z. This column concentration,  $c_{Br,col}(z) = \int_0^z c_{Br}(z') dz'$ , is graphed in Figure 7. The curves highlight how dodecyl sulfate depletes the interfacial region of Br ions while tetrahexylammonium enhances them with respect to pure 0.38 M NaBr. The steady parallel slopes at large depths for the three solutions containing NaBr result from integrating the 0.38 M bulk Br concentration, but the sharp increase in Br<sup>-</sup> for the THABr + NaBr solution arises from the pileup of subsurface Br ions. Over the full 70 Å depth encompassing the THABr depth profiles, the Br column concentration is 3.3 times larger when NaBr is added. At a narrower selected depth z of 10 Å, the column concentrations are (in units of 10<sup>13</sup> cm<sup>-2</sup>): 0.32 (SDS + NaBr), 1.9 (NaBr) 8.9 (THABr), and 9.9 (THABr + NaBr). These values yield a 31fold Br ratio for THABr/NaBr to SDS/NaBr, again reflecting the ability of THA<sup>+</sup> to attract Br<sup>-</sup> ions to the surface and of DS<sup>-</sup> to repel them. This ratio is not as high as the measured 70-fold



**Figure 7.** Br<sup>-</sup> column (depth integrated) concentrations at depths z from 0 to 80 Å, obtained from  $c_{\rm Br,col}(z) = \int_{-z}^{z} c_{\rm Br}(z') \, \mathrm{d}z'$  and the data in Figure 6. Both THABr solutions contain segregated Br<sup>-</sup> ions in the interfacial region, while the DS<sup>-</sup> interface is depleted in Br<sup>-</sup>. The curves for THABr + NaBr (red), NaBr (gray), and SDS + NaBr (green) become parallel at large depths because they are integrals of the same 0.38 M NaBr bulk concentration. The curve for THABr alone (black) is nearly flat at large depths because of its low 0.013 M bulk concentration.

increase in  $Br_2$  produced upon reaction of  $Br^-$  with  $Cl_2$ , suggesting that this halogen-exchange reaction may occur in a region even narrower than 10 Å.

Oxygen Depth Profiles and Interfacial Depletion of Glycerol Solvent. The O and C regions of the different He TOF spectra are shown in Figure 8 between 4400 and 6000 ns. Oxygen is found only in glycerol in the THABr + NaBr system, so that its depth profile corresponds to the solvent depth profile as well. The most prominent feature is the depletion of the oxygen edge for THABr + NaBr versus THABr. This lower signal implies that there are fewer solvent molecules in the

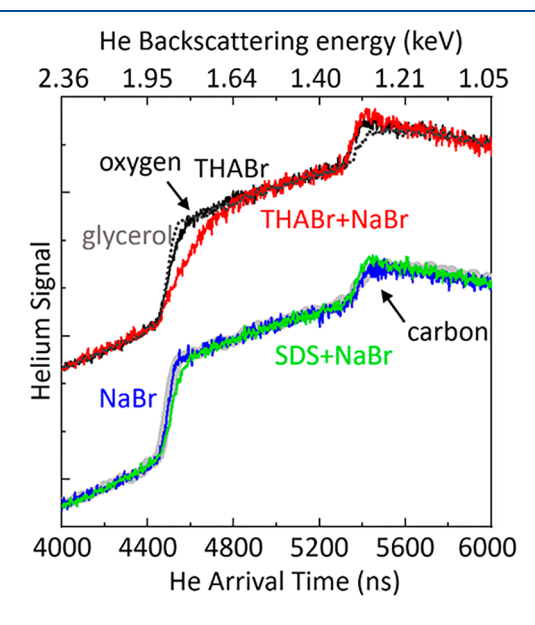
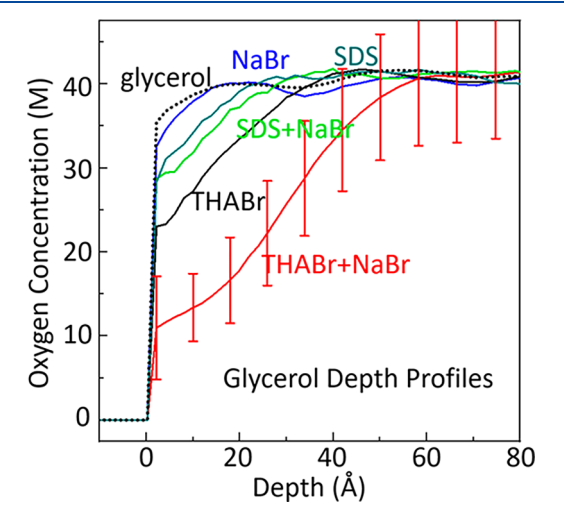


Figure 8. TOF spectra of He atoms backscattered from each solution in the He arrival time range for O and C atoms. Oxygen represents the glycerol solvent; notice its reduction as surface  $THA^+$  pushes the solvent to lower depths.

interfacial region. Figure 9 displays the deconvoluted oxygen (glycerol) concentration depth profiles for each solution, based



**Figure 9.** Deconvoluted oxygen depth profiles for each solution, where 3 O atoms = 1 glycerol molecule (roughly 41 M O atoms = 13.7 M glycerol). The wiggles are artifacts of the genetic algorithm. For the THABr + NaBr solution, glycerol solvent is severely depleted in the interfacial region because of pileup of THA $^+$  as the surfactant is salted out by added NaBr. The SDS profiles appear less depleted in part because of the four extra O atoms per sulfate group that fill in the interfacial region, and because DS $^-$  is smaller than THA $^+$ .

on Figure 8. The wiggles in the spectra are artifacts of the genetic algorithm, but the deconvoluted profiles still enable us to quantitatively determine the depletion of solvent in the outermost 70 Å of the solution. In particular, for THABr + NaBr, the glycerol concentration drops by 75% from 13.7 M (41 M oxygen atoms) in pure glycerol to just  $\sim$ 3.5 M. These spectra reflect the buildup of surface and subsurface THA<sup>+</sup> and Br<sup>-</sup> ions that push glycerol molecules into the bulk. The maximum 75% difference corresponds to ~10 M glycerol or 60 M oxygen and carbon atoms. This gap is filled by THA<sup>+</sup> and Br<sup>-</sup>, which at the 2 M maximum concentration in Figure 6 is crudely matched by ~52 M carbon and nitrogen atoms of THA+ and Br ions. Together, Figures 6 and 9 indicate that the THABr + NaBr solution generates a solvent-poor interfacial region composed of THA<sup>+</sup> and Br<sup>-</sup> ions that becomes increasingly diluted by solvent glycerol over 70 Å.

Surfactant Depth Profiles of C and S atoms of THA+ and DS-. NICISS is also capable of determining the distributions of the THA+ and DS- surfactants themselves. Unfortunately, nitrogen, the signature element of THA+, is too difficult to detect because of its relatively low concentration and small collision cross section. However, we can detect THA+ at least approximately because its buildup at the surface creates a dense carbon layer. Figure 10a shows the C and O signals in the THABr + NaBr solution, where the O signal represents just the glycerol solvent (and its C atoms); 11 the difference between them is the He scattering signal from C atoms in THA<sup>+</sup> (see the Supporting Information for determining the depth scale of the carbon density profile). The deconvoluted difference spectra are graphed in Figure 10b for both 0.013 M THA<sup>+</sup> and for 0.013 M THA+ + 0.38 M NaBr. They are plotted along with the corresponding Br spectra, which is nearly identical for 0.013 M THABr, corresponding to a fwhm of  $\sim$ 10 Å. This is just the size of a THA<sup>+</sup> ion and suggests that the associated Br<sup>-</sup> ions in Figure

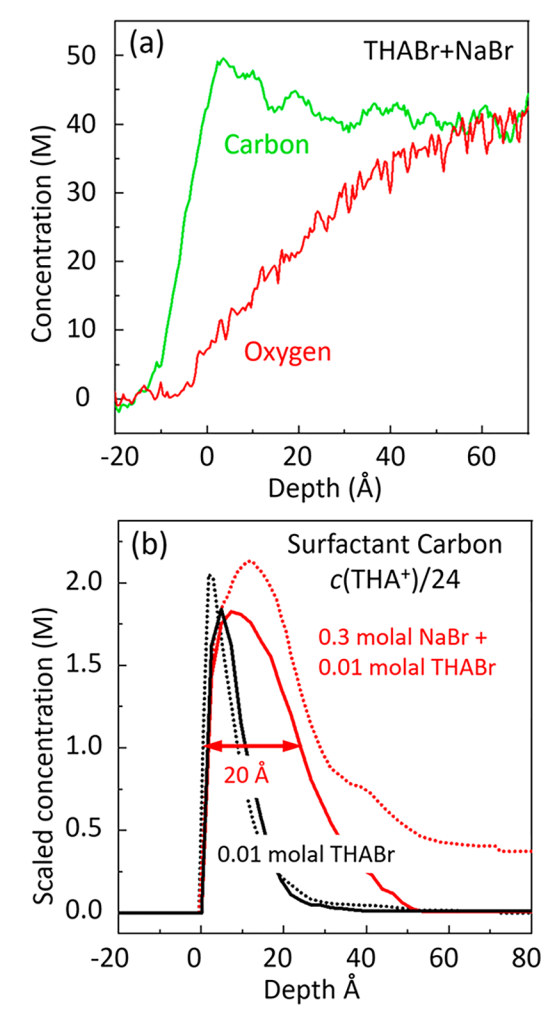


Figure 10. (a) Isolating the carbon signal of  $THA^+$  from glycerol in the THABr + NaBr solution. The carbon spectrum is the sum of  $THA^+$  and glycerol C atoms, while the oxygen spectrum arises just from glycerol. (b) Deconvoluted depth profiles of carbon (solid) and of bromine (dotted) in the THABr (black) and THABr + NaBr (red) solutions, obtained by dividing the carbon concentration by 24 carbon atoms per  $THA^+$  ion.

5 may locate themselves along the span of the surface THA<sup>+</sup> ions. Intriguingly, this observation is in accord with electronic structure calculations, which suggest that the charge on tetraalkyl ions is not localized on the N atom but is instead distributed over the CH<sub>2</sub> groups, smearing the charge attracting the Br<sup>-</sup> over part of the hexyl chains.<sup>55</sup> The overlapping THA<sup>+</sup> and Br<sup>-</sup> depth profiles of pure THABr in Figure 10b are also in accord with previous studies of similar tetrabutylphosphonium and halide ion depth profiles in formamide.<sup>5</sup>

Figure 10b further demonstrates that the integrated number of THA<sup>+</sup> ions increases by 2.2-fold and are spread over 20 Å (fwhm) upon adding NaBr, equal to at least two THA<sup>+</sup> diameters. This profile is just slightly narrower than the corresponding Br<sup>-</sup> profile shown in the figure and corroborates the inference that the salting out of the surfactant is more than just one layer thick. The displacement of organic ions to the surface by added salt has been observed in numerous surface tension, <sup>8,10,56-60</sup> neutron reflectivity, <sup>61,62</sup> spectroscopic, <sup>63</sup> and simulations <sup>64,65</sup> studies before. It is often attributed to a reduction in charge repulsion between the ionic surfactant headgroups by counterions from the salt that intersperse

between the headgroups. 58,65 Together, Figures 6 and 10 give a multilayer length scale to this surfactant exclusion. 19 A reviewer pointed out to us a fascinating parallel to the Jones—Ray effect (a decrease in surface tension at millimolar salt concentrations), which has been explained by the presence of submicromolar concentrations of ionic surfactants that accumulate at the surface because of a similar screening by added salt. 66,67

The large collision cross section of the sulfur atom enables interfacial DS<sup>-</sup> ions to be detected directly by NICISS, as shown in Figure 11. This plot reveals that Na<sup>+</sup> ions are visible as a

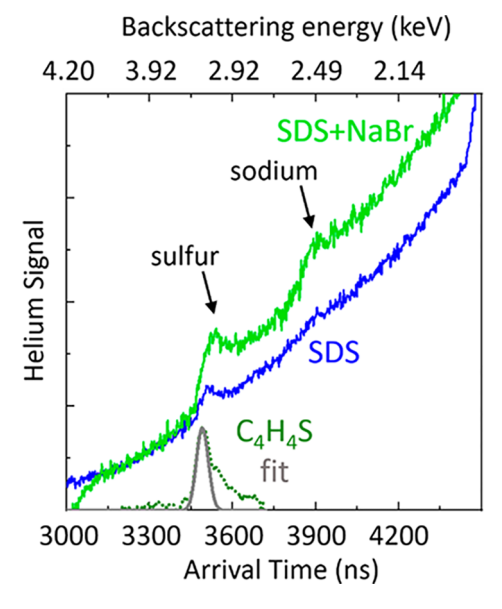


**Figure 11.** TOF spectra of He atoms backscattering from SDS and SDS + NaBr solutions in the region of S and Na atoms. The gas-phase thiophene spectrum is also shown, along with a Gaussian fit used for deconvolution.

shoulder. Figure 11 also contains the spectrum of gas-phase thiophene, which is unexpectedly broad. We speculate that the tail at longer arrival times arises primarily from He<sup>+</sup> ions striking thiophene on the end opposite the sulfur atom, thus losing extra energy in collisions with carbon atoms before scattering from the sulfur atom. As indicated in the figure, we use only the highenergy component for deconvolution. Note that the sulfur peak is delayed with respect to the gas-phase peak; this reflects the S atom position at the end of the dodecyl chain, which must be traversed by the He atom before colliding with the S atom itself.

The deeper positions of the S atom are evident in the deconvoluted spectra in Figure 12, which compare the sulfur depth profiles for pure 0.0065 M SDS and with added 0.38 M NaBr. A significant difference from the THABr solutions is that the addition of 0.38 M NaBr increases the peak surfactant concentration as well as its depth into solution. The single-chain dodecyl sulfate ion packs more tightly than does the bulkier tetrahexylammonium ion, and at close packing occupies roughly 20 Å<sup>2</sup> area per molecule over a length of 18 Å.<sup>15</sup> These parameters correspond to a maximum surface concentration of 5  $\times$  10<sup>14</sup> cm<sup>-2</sup> and a volume of 360 Å<sup>3</sup> per chain or a volume concentration of 4.6 M. This maximum packing is not achieved in water because of micelle formation, which limits surface concentrations to  $3 \times 10^{14}$  cm<sup>-2</sup> or 2.8 M. Figure 12 reveals that the addition of NaBr increases the DS- surface concentration from 1.2 to 2.2 M, well below maximum possible packing.

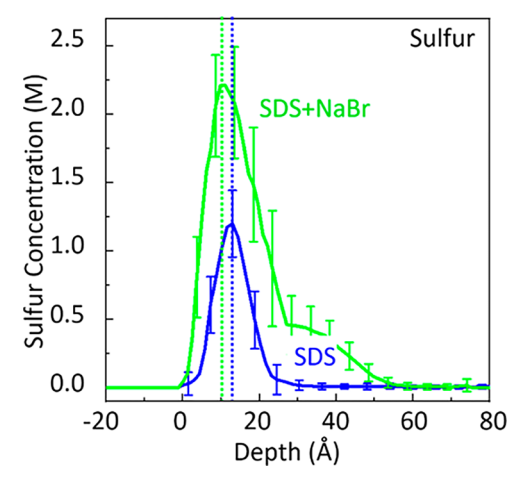


**Figure 12.** Sulfur deconvoluted depth profiles for 0.0064 M SDS and 0.0064 M SDS + 0.38 M NaBr. The error bars represent  $\pm$  one standard deviation of 10000 trials generated by the genetic algorithm. In contrast to Figure 10, the addition of NaBr increases both the peak concentration of DS<sup>-</sup> ions as well as their range of depths in solution.

The depth axis for the uppermost ~20 Å in Figure 12 is uncertain because the incomplete DS<sup>-</sup> layer has a lower density than a bulk liquid and therefore the He atoms lose less energy per angstrom (lower stopping power) as they travel through the surfactant layer. This in turn implies that the depth scale should be stretched and the concentration axis shrunk in the interfacial region to maintain constant area. This scaling is currently unknown but could be determined if the average DS<sup>-</sup> chain length was measured for example, by neutron scattering. Applying the current stopping power to Figure 12, the average S atom is submersed by about 12 Å, smaller than the maximum 18 Å extension of the dodecyl chain, suggesting that the chains are not in all trans positions. These bent configurations and headgroup distributions are also observed in simulations, <sup>23,68</sup> suggesting that the depth scale may be approximately correct.

The ability to detect C, O, S,  $Na^+$ , and  $Br^-$  in the SDS + NaBr solution provides the opportunity to map out in detail the behavior of each species in a solution combining surfactant and salt. These depth profiles are collected in Figure 13, subject to the uncertainty in the stopping power near the outermost surface region, with particularly poor knowledge of the positioning of the  $Na^+$  profile of  $\pm 8$  Å (as calculated in the Supporting Information). As anticipated, the carbon chain appears first, followed in order by sulfur, sodium, <sup>69</sup> oxygen, and then bromide, which is repelled from the interfacial region. The broad distribution of S atoms implies that the sulfate charge is also spread over at least 35 Å, matching the depletion of  $Sr^-$  ions. The associated chain immersion into the glycerol subphase has been previously observed in water by neutron reflectivity <sup>15</sup> and computer simulations. <sup>23,68</sup>

Lastly, we note that the depth profiles in Figures 6, 10, 12, and 13 may be used to extract the Gibbs relative surface excesses for each element. Comparisons with excesses calculated from surface tensions are made in Appendix II; they agree within 35% for pure THABr and SDS solutions but substantially underestimate the integrated NICISS profiles when NaBr is added. Two possible explanations include incomplete wetting of the Pt plate for surface tension measurements and ignorance of accurate activity coefficients for the Gibbs analysis. 70

Concluding Remarks: Surfactant Salting Out and Control of Interfacial Br<sup>-</sup> Depth Profiles. The two chief

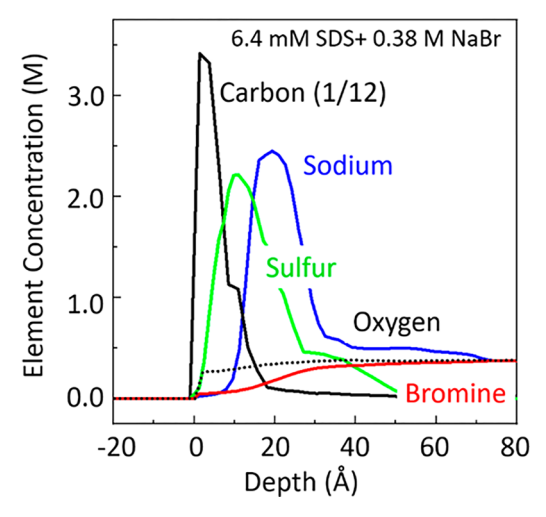


Figure 13. Complete map of species in the 0.0064 M SDS + 0.38 M NaBr solution. The ordering of the elements C (black), S (green), Na<sup>+</sup> (blue), and Br (red) follow expectations for the positions of the dodecyl chains in the outermost region and S atoms closer to the surface, matched with its associated Na+ counterions. Bromide ions (red) are repelled by the segregated DS ions, while the glycerol and sulfate oxygens (dotted line) occupy locations up through the headgroup position. The oxygen curve is normalized to the bulk Brconcentration for ease of comparison. See the Supporting Information for uncertainties in the positioning of the Na<sup>+</sup> profile.

results in this study involve the "salting out" of ionic surfactants to the surface and the correlation between interfacial Br composition and interfacial reactivity. Figure 6 demonstrates that the addition of 0.30 m NaBr to 0.010 m THABr increases the Br and THA concentrations by roughly 3-fold and broadens the widths of these ion regions from  $\sim 10$  to  $\sim 30$  Å. This segregation of THA<sup>+</sup> from the bulk primarily causes THA<sup>+</sup> and its Br counterions to "pile" up in a multilayer region spanning about three THA+ ions or six glycerol solvent molecules. Figure 13 also reveals bunching up of Na<sup>+</sup> and DS<sup>-</sup> ions, which collect in a similarly broad interfacial region upon adding NaBr. As implied by Figures 6, 7, and 9, this bunching creates regions that are composed more of surfactant and inorganic ions than of solvent molecules. It will be intriguing to learn in future studies how this ion bunching and their depth profiles can be tuned by varying the identity and concentration of added salt, and if they can be predicted by electrostatic models that invoke counterions localized within the surfactant ion region. 5,8,10,32,60,66,67,71

A second key outcome of the density profiles is the remarkable change in Br concentrations with cationic and anionic surfactants. Integrated over a 10 Å depth in Figure 7, the Br concentration ratio drops by 30-fold from THABr + NaBr to SDS + NaBr, likely because THA+ attracts Br- ions and DSrepels them. This large ratio is close to the measured change in reactivity of Cl<sub>2</sub> with Br<sup>-</sup>, which dropped by 70-fold upon substitution of SDS for THABr. One implication of this abruptly changing interfacial Br concentration is that the headgroup, rather than the alkyl chain, primarily controls access to the halide ion in porous surfactant films. 44,72 In particular, the depth profiles indicate that the  $Cl_2 + 2 Br^- \rightarrow Br_2 + 2Cl^-$  reaction most likely takes place within the outermost 1-2 monolayers of the THABr/NaBr and SDS/NaBr solutions in order to access such a wide range of Br concentrations. This region of enhanced reactivity is not like bulk glycerol but is a mixture of ~3 M

glycerol molecules and ~2 M THA+ and Br ions in the THABr/NaBr solution. If similar results hold for Cl<sup>-</sup> ions, these studies imply a fascinating role for cationic surfactants in other aerosol-mediated reactions in the atmosphere, such as  $N_2O_5(g)$ +  $Cl^- \rightarrow ClNO_2(g) + NO_3^-$ . Our preliminary studies of THABr in NaCl/NaBr mixtures in glycerol suggest that Cl<sup>-</sup> ions indeed segregate to the surface, although not to the extent that Br ions

# APPENDIX I: TESTS AND IMPLICATIONS OF NA<sup>+</sup>, BR-, AND SURFACTANT ION **ELECTRONEUTRALITY**

The Br<sup>-</sup>, Na<sup>+</sup>, THA<sup>+</sup>, and DS<sup>-</sup> depth profiles can be used to verify electroneutrality in the interfacial region.<sup>31</sup> Figures 6, 9, and 13 indicate that the depth profiles converge to their bulk concentrations at a cutoff depth of 70 Å. Table A.1 summarizes

Table A.1. Electroneutrality in the Interfacial Region (Column Concentrations<sup>a</sup> from 0 to 70 Å in Units of  $1 \times 10^{13}$ molecules cm<sup>-2</sup>)

co-ion		surfactant	counterion					
12 mM THABr								
		$c(\mathrm{THA}^{\scriptscriptstyle +})$	=	$c(Br^{-})$				
		$1/24 \times c(C_{\text{surfactant}})$	=	$c(Br^{-})$				
		12.6	$\approx$	13.2				
12 mM THABr + 0.3 M NaBr								
$c(Na^+)$	+	$c(\mathrm{THA^+})$	=	$c(Br^-)$				
$c(Na^+)$	+	$1/24 \times c(C_{\text{surfactant}})$	=	$c(Br^{-})$				
?	+	28	$\approx$	44				
6 mM SDS								
		$c(DS^-)$	=	$c(Na^+)$				
		$c(S)$ or $1/12 \times c(C_{surfactant})$	=	$c(Na^+)$				
		8.6 or 6	$\approx$	7.5				
6 mM SDS + 0.3 M NaBr								
$c(Br^{-})$	+	$c(DS^-)$	=	$c(Na^+)$				
$c(Br^{-})$	+	$c(S)$ or $1/12 \times c(C_{surfactant})$	=	$c(Na^+)$				
10.8	+	26 or 23	$\approx$	35				

<sup>a</sup>Column concentrations =  $c_{col}(z=70\text{Å}) = \int_0^z c(z') dz'$  obtained from Figure 7.

these integrals for all species and generally validates the NICISS technique. For 0.13 M THABr, the column concentrations of the ions THA<sup>+</sup> and Br<sup>-</sup> are equal within 5%. For DS<sup>-</sup>, the column concentrations may be calculated directly using the sulfur or carbon atom spectra: the average value of the DScolumn concentrations equals the Na<sup>+</sup> concentration within 3%. Similarly, in the SDS + NaBr system, the positive and negative ion concentrations agree within 1%.

The 0.013 M THABr + 0.38 M NaBr solution could unfortunately not be tested for electroneutrality because Na+ could not be discerned in the NICISS spectra. However, to achieve neutrality, the Na<sup>+</sup> column concentration must be close to  $16 \times 10^{13}$  cm<sup>-2</sup>, which is similar to Na<sup>+</sup> concentration in 0.35 M NaBr alone. This surprising result implies that the addition of NaBr to THABr forces extra THA+ and Br to the interfacial region but does not reduce the Na+ concentration, in contrast to the mirror situation in which Br is strongly depleted by the addition of NaBr to SDS. One possible explanation is that Br ions specifically bind to surface THA+ within the hydrophobic pocket created by the hexyl chains; 73 this tight ion pairing may in turn reduce charge repulsion between Na<sup>+</sup> and THA<sup>+</sup>, allowing Na<sup>+</sup> to remain in the interfacial region.

# APPENDIX II: SURFACE TENSION AND NICISS DETERMINATIONS OF SURFACE ADSORPTIONS

The Gibbs relative surface excess obtained from measurements of surface tension  $\gamma$  versus solute activity  $f_\pm c_{\rm solute}$  may also be calculated from NICISS experiments according to

$$\Gamma_{\text{solute}}^{\text{glycerol}} = -\frac{1}{mRT} \left( \frac{\partial \gamma}{\partial \ln f_{\pm} c_{\text{solute}}} \right)_{T}$$

$$= \int_{0}^{70\text{Å}} \left[ c_{\text{solute}}(z) - \frac{c_{\text{solute}}^{\text{bulk}}}{c_{\text{plycerol}}} c_{\text{glycerol}}(z) \right] dz$$

where  $m=1+c({\rm THABr~or~SDS})/(c({\rm THABr~or~SDS})+c({\rm NaBr})).^8$  We have previously reported surface tension measurements of the systems studied here using the Wilhelmy method and a Pt plate. 44,74,75 They are summarized in Table A.2, along with the NICISS integrations. The upper limit of 70 Å was chosen because all profiles converge to their bulk concentrations at this depth.

Table A.2. Relative Surface Excess  $\Gamma_{solute}^{glycerol}$  in Units of  $10^{13}$  cm<sup>-2</sup>

solution/ technique	NICISS THA <sup>+</sup> or DS <sup>-</sup>	NICISS counterion Br <sup>-</sup> or Na <sup>+</sup>	NICISS co- ion Na <sup>+</sup> or Br <sup>-</sup>	surface tension			
0.0050 m SDS	6/8.6 (S)	7.5	no co-ion	6 <sup>a</sup>			
0.0050 m SDS + 0.30 m NaBr	23/26(S)	31	-3.8 Br <sup>-</sup>	12 <sup>b</sup>			
$0.010\ m\ \mathrm{THABr}$	12.6 (C)	13	no co-ion	$9^c$			
0.010 m THABr + 0.30 m NaBr	28 (C)	33	Na <sup>+</sup> not detected	10 <sup>a</sup>			
<sup>a</sup> Reference 75. <sup>b</sup> Reference 44. <sup>c</sup> Reference 74.							

Table A.2 shows that the surface tension and NICISS measurements agree within 35% for 0.010 *m* THABr and 0.0050 *m* SDS, but they substantially underestimate the NICISS values when 0.30 *m* NaBr is added. We do not have an explanation for this disagreement but suspect that the surface tension measurements were not carried out correctly. Three reasons include erroneously measured detachment forces of the Pt plate, incomplete wetting of the plate, and strongly changing activity coefficients due to bulk-phase aggregation. The latter two effects and others are described by Li, Thomas, and Penfold, who have been especially critical of plate-based surface tension measurements at high surfactant concentrations. We hope that further measurements, such as neutron reflectivity or non-plate surface tension measurements, will provide an independent test of the NICISS technique in salt-surfactant solutions.

# ASSOCIATED CONTENT

### Supporting Information

The Supporting Information is available free of charge at https://pubs.acs.org/doi/10.1021/acs.jpcb.9b11686.

Description of conversion of helium atom arrival time to He backscattering energy and then to depth of the target element and determining the He backscattering energy at zero depth for elements in the absence of gas-phase measurements (PDF)

### AUTHOR INFORMATION

### **Corresponding Authors**

Xianyuan Zhao — Department of Chemistry, University of Wisconsin—Madison, Madison, Wisconsin 53706, United States; Occid.org/0000-0001-7926-6562;

Email: xzhao287@wisc.edu

Gilbert M. Nathanson — Department of Chemistry, University of Wisconsin—Madison, Madison, Wisconsin 53706, United States; orcid.org/0000-0002-6921-6841; Email: gmnathan@wisc.edu

**Gunther G. Andersson** — Institute for Nanoscale Science and Technology, Flinders University, Adelaide, SA 5001, Australia;

orcid.org/0000-0001-5742-3037; Email: gunther.andersson@flinders.edu.au

Complete contact information is available at: https://pubs.acs.org/10.1021/acs.jpcb.9b11686

### Notes

The authors declare no competing financial interest.

## ACKNOWLEDGMENTS

We are grateful to the National Science Foundation for supporting this research via the Center for Aerosol Impacts on Chemistry of the Environment, a NSF Center for Chemical Innovation (NSF CHE 1801971). We also thank the reviewers for their insightful comments. The authors acknowledge the support of the Australian National Fabrication Facility (ANFF) and Australian Microscopy & Microanalysis Research Facility (AMMRF) regarding the use of experimental equipment. The authors further acknowledge Flinders Microscopy and Microanalysis and their expertise. We also thank Christopher Price and Andre Dunn for their support in machining and electronics design, and thank Liam Howard-Fabretto and Anand Kumar for their assistance with instrumentation.

### REFERENCES

- (1) Eschen, F.; Heyerhoff, M.; Morgner, H.; Vogt, J. The Concentration Depth Profile at the Surface of a Solution of Tetrabutyammonium Iodide in Formamide, Based on Angle-Resolved Photoelectron Spectroscopy. *J. Phys.: Condens. Matter* **1995**, *7*, 1961–1978.
- (2) Su, T. J.; Lu, J. R.; Thomas, R. K.; Penfold, J. Neutron Reflection from Counterions at the Surface of a Soluble Surfactant Solution. *J. Phys. Chem. B* **1997**, *101*, 937–943.
- (3) Winter, B.; Weber, R.; Schmidt, P. M.; Hertel, I. V.; Faubel, M.; Vrbka, L.; Jungwirth, P. Molecular Structure of Surface-Active Salt Solutions: Photoelectron Spectroscopy and Molecular Dynamics Simulations of Aqueous Tetrabutylammonium Iodide. *J. Phys. Chem. B* **2004**, *108*, 14558–14564.
- (4) Andersson, G.; Krebs, T.; Morgner, H. Angle Resolved Ion Scattering Spectroscopy Reveals the Local Topography Around Atoms in a Liquid Surface. *Phys. Chem. Chem. Phys.* **2005**, *7*, 2948–2954.
- (5) Schulze, K. D.; Morgner, H. Investigation of the Electric Charge Structure and the Dielectric Permittivity at Surfaces of Solutions Containing Ionic Surfactants. *J. Phys.: Condens. Matter* **2006**, *18*, 9823–9839.
- (6) Abranko-Rideg, N.; Horvai, G.; Jedlovszky, P. Structure of the Adsorption Layer of Various Ionic and Non-Ionic Surfactants at the Free Water Surface, as Seen from Computer Simulation and ITIM Analysis. J. Mol. Liq. 2015, 205, 9–15.
- (7) Kalra, A.; Tugcu, N.; Cramer, S. M.; Garde, S. Salting-in and Salting-Out of Hydrophobic Solutes in Aqueous Salt Solutions. *J. Phys. Chem. B* **2001**, *105*, 6380–6386.
- (8) Chattoraj, D. K.; Birdi, K. S. Adsorption and the Gibbs Surface Excess; Plenum Press, 1984.

- (9) Jungwirth, P.; Tobias, D. J. Specific Ion Effects at the Air/Water Interface. *Chem. Rev.* **2006**, *106*, 1259–1281.
- (10) Prosser, A. J.; Franses, E. I. Adsorption and Surface Tension of Ionic Surfactants at the Air-Water Interface: Review and Evaluation of Equilibrium Models. *Colloids Surf.*, A **2001**, *178*, 1–40.
- (11) Andersson, G.; Krebs, T.; Morgner, H. Activity of Surface Active Substances Determined from Their Surface Excess. *Phys. Chem. Chem. Phys.* **2005**, *7*, 136–142.
- (12) Baschenko, O. A.; Bokman, F.; Bohman, O.; Siegbahn, H. O. G. Distribution of Ions in Subsurface Layers of Liquid Solutions Studied by ARXPS. *J. Electron Spectrosc. Relat. Phenom.* **1993**, *62*, 317–334.
- (13) Ghosal, S.; Hemminger, J. C.; Bluhm, H.; Mun, B. S.; Hebenstreit, E. L. D.; Ketteler, G.; Ogletree, D. F.; Requejo, F. G.; Salmeron, M. Electron Spectroscopy of Aqueous Solution Interfaces Reveals Surface Enhancement of Halides. *Science* **2005**, *307*, 563–566.
- (14) Krisch, M. J.; D'Auria, R.; Brown, M. A.; Tobias, D. J.; Hemminger, J. C.; Ammann, M.; Starr, D. E.; Bluhm, H. The Effect of an Organic Surfactant on the Liquid-Vapor Interface of an Electrolyte Solution. *J. Phys. Chem. C* **2007**, *111*, 13497–13509.
- (15) Lu, J. R.; Simister, E. A.; Lee, E. M.; Thomas, R. K.; Rennie, A. R.; Penfold, J. Direct Determination by Neutron Reflection of the Penetration of Water into Surfactant Layers at the Air/Water Interface. *Langmuir* 1992, *8*, 1837–1844.
- (16) Lu, J. R.; Li, Z. X.; Smallwood, J.; Thomas, R. K.; Penfold, J. Detailed Structure of the Hydrocarbon Chain in a Surfactant Monolayer at the Air-Water Interface Neutron Reflection from Hexadecyltrimethyl ammonium bromide. *J. Phys. Chem.* **1995**, *99*, 8233–8243.
- (17) Sloutskin, E.; Baumert, J.; Ocko, B. M.; Kuzmenko, I.; Checco, A.; Tamam, L.; Ofer, E.; Gog, T.; Gang, O.; Deutsch, M. The Surface Structure of Concentrated Aqueous Salt Solutions. *J. Chem. Phys.* **2007**, *126*, No. 054704.
- (18) Luo, G. M.; Bu, W.; Mihaylov, M.; Kuzmenko, I.; Schlossman, M. L.; Soderholm, L. X-ray Reflectivity Reveals a Nonmonotonic Ion-Density Profile Perpendicular to the Surface of ErCl<sub>3</sub> Aqueous Solutions. *J. Phys. Chem. C* **2013**, *117*, 19082–19090.
- (19) See also: Thomas, R. K.; Penfold, J. Multilayering of Surfactant Systems at the Air-Dilute Aqueous Solution Interface. *Langmuir* **2015**, 31, 7440–7456.
- (20) Andersson, G.; Ridings, C. Ion Scattering Studies of Molecular Structure at Liquid Surfaces with Applications in Industrial and Biological Systems. *Chem. Rev.* **2014**, *114*, 8361–8387.
- (21) Hua, W.; Verreault, D.; Allen, H. C. Relative Order of Sulfuric Acid, Bisulfate, Hydronium, and Cations at the Air-Water Interface. *J. Am. Chem. Soc.* **2015**, *137*, 13920–13926.
- (22) Jungwirth, P.; Winter, B. Ions at Aqueous Interfaces: From Water Surface to Hydrated Proteins. *Annu. Rev. Phys. Chem.* **2008**, *59*, 343–366.
- (23) Rideg, N. A.; Darvas, M.; Varga, I.; Jedlovszky, P. Lateral Dynamics of Surfactants at the Free Water Surface: A Computer Simulation Study. *Langmuir* **2012**, *28*, 14944–14953.
- (24) Andersson, G.; Morgner, H. Impact Collision Ion Scattering Spectroscopy (ICISS) and Neutral Impact Collision Ion Scattering Spectroscopy (NICISS) at Surfaces of Organic Liquids. *Surf. Sci.* **1998**, 405, 138–151.
- (25) Andersson, G.; Morgner, H. Thermodynamics and Structure of Liquid Surfaces Investigated Directly with Surface Analytical Tools. *Ann. Phys.* **2017**, 529, 1600230.
- (26) Andersson, G.; Morgner, H.; Cwiklik, L.; Jungwirth, P. Anions of Alkali Halide Salts at Surfaces of Formamide Solutions: Concentration Depth Profiles and Surface Topography. *J. Phys. Chem. C* **2007**, *111*, 4379–4387.
- (27) Ishiyama, T.; Morita, A. Molecular dynamics Study of Gas-Liquid Aqueous Sodium Halide Interfaces. I. Flexible and Polarizable Molecular Modeling and Interfacial Properties. *J. Phys. Chem. C* **2007**, *111*, 721–737.
- (28) Stern, A. C.; Baer, M. D.; Mundy, C. J.; Tobias, D. J. Thermodynamics of Iodide Adsorption at the Instantaneous Air-Water Interface. *J. Chem. Phys.* **2013**, *138*, 114709.

- (29) Perrine, K. A.; Parry, K. M.; Stern, A. C.; Van Spyk, M. H. C.; Makowski, M. J.; Freites, J. A.; Winter, B.; Tobias, D. J.; Hemminger, J. C. Specific Cation Effects at Aqueous Solution-Vapor Interfaces: Surfactant-Like Behavior of Li<sup>+</sup> Revealed by Experiments and Simulations. *Proc. Natl. Acad. Sci. U. S. A.* **2017**, *114*, 13363–13368.
- (30) Li, J. C.; Wang, F. Surface Penetration without Enrichment: Simulations Show Ion Surface Propensities Consistent with Both Elevated Surface Tension and Surface Sensitive Spectroscopy. *J. Phys. Chem. B* **2019**, 123, 7197–7203.
- (31) Andersson, G.; Morgner, H. Investigations on Solutions of Tetrabutylammonium Salts in Formamide with NICISS and ICISS: Concentration Depth Profiles and Composition of the Outermost Layer. Surf. Sci. 2000, 445, 89–99.
- (32) Wang, C. Y.; Morgner, H. Effects of Counterions on Adsorption Behavior of Anionic Surfactants on Solution Surface. *Langmuir* **2010**, 26, 3121–3125.
- (33) Ridings, C.; Stubenrauch, C.; Andersson, G. G. Effect of Sodium Halides on the Surface Structure of Foam Films Stabilized by a Nonionic Surfactant. *J. Phys. Chem. C* **2015**, *119*, 441–448.
- (34) Andersson, G. Energy-Loss Straggling of Helium Projectiles at Low Kinetic Energies. *Phys. Rev. A: At., Mol., Opt. Phys.* **2007**, 75, No. 032901.
- (35) Andersson, G.; Morgner, H.; Pohl, H. Energy-Loss Straggling of Helium Projectiles at Low Kinetic Energies: Deconvolution of Concentration Depth Profiles of Inorganic Salt Solutes in Aqueous Solutions. *Phys. Rev. A: At., Mol., Opt. Phys.* **2008**, 78, No. 032904.
- (36) Andersson, G.; Morgner, H. Determining the Stopping Power of Low Energy Helium in Alkanethiolates with Neutral Impact Collision Ion Scattering Spectroscopy (NICISS). *Nucl. Instrum. Methods Phys. Res., Sect. B* **1999**, *155*, 357–368.
- (37) See model calculations at "The Stopping and Range of Ions in Matter" at www.SRIM.org by J. F. Ziegler. No experiments exist yet to corroborate these predictions at 5 keV He collision energy. The 15% predicted increase in stopping power was therefore not incorporated into our analysis. We emphasize that a 15% larger stopping power will shrink that depth scale for all elemental profiles by the same fraction and therefore does not shift their relative positions. Our best estimate is an even smaller correction, as a recent NICISS study of an oxygen-rich lipid bilayer yields the same depth as measured by neutron scattering. See ref 38.
- (38) Alharbi, A. R. M.; Andersson, J. M.; Koper, I.; Andersson, G. G. Investigating the Structure of Self-Assembled Monolayers Related to Biological Cell Membranes. *Langmuir* **2019**, 35, 14213–14221.
- (39) Benjamin, I. Chemical Reactions and Solvation at Liquid Interfaces: A Microscopic Perspective. *Chem. Rev.* **1996**, *96*, 1449–1475.
- (40) Bresme, F.; Chacon, E.; Tarazona, P.; Wynveen, A. The Structure of Ionic Aqueous Solutions at Interfaces: An Intrinsic Structure Analysis. *J. Chem. Phys.* **2012**, *137*, 114706.
- (41) Oh-e, M.; Yokoyama, H.; Baldelli, S. Structure of the Glycerol Liquid/Vapor Interface Studied by Sum-Frequency Vibrational Spectroscopy. *Appl. Phys. Lett.* **2004**, *84*, 4965–4967.
- (42) Benjamin, I.; Wilson, M.; Pohorille, A. Scattering of Ne from the Liquid-Vapor Interface of Glycerol A Molecular Dynamics Study. *J. Chem. Phys.* **1994**, *100*, 6500–6507.
- (43) Wiens, J. P.; Nathanson, G. M.; Alexander, W. A.; Minton, T. K.; Lakshmi, S.; Schatz, G. C. Collisions of Sodium Atoms with Liquid Glycerol: Insights into Solvation and Ionization. *J. Am. Chem. Soc.* **2014**, 136, 3065–3074.
- (44) Gord, J. R.; Zhao, X.; Liu, E.; Bertram, T. H.; Nathanson, G. M. Control of Interfacial  $\text{Cl}_2$  and  $\text{N}_2\text{O}_5$  Reactivity by a Zwitterionic Phospholipid in Comparison with Ionic and Uncharged Surfactants. *J. Phys. Chem. A* **2018**, *122*, 6593–6604.
- (45) Spitzl, R.; Niehus, H.; Comsa, G. 180-Degrees Low-Energy Impact Collision Ion-Scattering Spectroscopy. *Rev. Sci. Instrum.* **1990**, *61*, 760–764.
- (46) We learned after the experiments were completed that the 0.010 m THABr + 0.30 m NaBr solution forms visibly spotty films when left standing on the benchtop. The solution, however, remains homoge-

- neous for 1 day after mild heating is used to dissolve the surfactant and degas and dewater the solution. The NICISS experiments were conducted during this time interval. The experiments themselves show that these films were not present on the continuously scraped coated wheel because the surfactant depth profiles reach their bulk phase value by 80 Å. The SDS solutions do not show this behavior and remain homogeneous and spot-free.
- (47) The time t for segregation of a bulk-phase surfactant is roughly given by  $t \approx (c_{\rm surf}/c_{\rm bulk})^2/D$ , where  $c_{\rm bulk} = 0.013$  M ( $\sim 10^{19}$  cm $^{-3}$ ),  $c_{\rm surf} \sim 10^{14}$  cm $^{-2}$ , and  $D \sim 10^{-8}$  cm $^2$  s $^{-1}$ . These numbers yield  $t \approx 0.01$  s, significantly shorter than the 3 s surface renewal time.
- (48) Andersson, G.; Morgner, H.; Schulze, K. D. Surface properties of electrolyte solutions studied with ion beam analysis. *Nucl. Instrum. Methods Phys. Res., Sect. B* **2002**, *190*, 222–225.
- (49) The deconvolution routine incorporates a weak (less than 10%) dependence of  $({\rm d}\sigma(z)/{\rm d}\omega)_{\rm Br}$  on z through the change in He kinetic energy with depth over 0 to 70 Å.
- (50) White, C. W.; Thomas, E. W.; van der Weg, W. F.; Tolk, N. H., Opical Emission from Low-Energy Ion-Surface Collisions. In *Inelastic Ion-Surface Collisions*; Tolk, N. H., Tully, J. C., Heiland, W., White, C. W., Eds.; Academic Press: New York, 1977.
- (51) Wang, C. Y.; Andersson, G. G. Measuring Concentration Depth Profiles at Liquid Surfaces: Comparing Angle Resolved X-Ray Photoelectron Spectroscopy and Neutral Impact Collision Scattering Spectroscopy. Surf. Sci. 2011, 605, 889–897.
- (52) Robinson, R. A.; Stokes, R. H. *Electrolyte Solutions*, 2nd ed.; Academic Press: New York, 1959; Chapter 14. We note that the factor of 2 is not included in other definitions of the Bjerrum length. See this text for its justification.
- (53) Marcus, Y. Tetraalkylammonium Ions in Aqueous and Non-Aqueous Solutions. *J. Solution Chem.* **2008**, *37*, 1071–1098.
- (\$4) Zhao, Y. H.; Abraham, M. H.; Zissimos, A. M. Determination of McGowan Volumes for Ions and Correlation with van der Waals Volumes. J. Chem. Inf. Comput. Sci. 2003, 43, 1848–1854.
- (55) Heyda, J.; Lund, M.; Oncak, M.; Slavicek, P.; Jungwirth, P. Reversal of Hofmeister Ordering for Pairing of NH<sub>4</sub><sup>+</sup> vs Alkylated Ammonium Cations with Halide Anions in Water. *J. Phys. Chem. B* **2010**, *114*, 10843–10852.
- (56) Okuda, H.; Imae, T.; Ikeda, S. The Adsorption of Cetytrimethylammonium Bromide on Aqueous Surfaces of Sodium-Bromide Solutions. *Colloids Surf.* **1987**, *27*, 187–200.
- (57) Tanaka, A.; Ikeda, S. Adsorption of Dodecyltrimethylammonium Bromide on Aqueous Surfaces of Sodium Bromide Solutions. *Colloids Surf.* **1991**, *56*, 217–228.
- (\$8) See review in: Para, G.; Jarek, E.; Warszynski, P.; Adamczyk, Z. Effect of Electrolytes on Surface Tension of Ionic Surfactant Solutions. *Colloids Surf., A* **2003**, 222, 213–222.
- (59) Gurkov, T. D.; Dimitrova, D. T.; Marinova, K. G.; Bilke-Crause, C.; Gerber, C.; Ivanov, I. B. Ionic Surfactants on Fluid Interfaces: Determination of the Adsorption; Role of the Salt and the Type of the Hydrophobic Phase. *Colloids Surf., A* **2005**, *261*, 29–38.
- (60) Para, G.; Jarek, E.; Warszyński, P. The surface Tension of Aqueous Solutions of Cetyltrimethylammonium Cationic Surfactants in Presence of Bromide and Chloride Counterions. *Colloids Surf., A* **2005**, *261*, *65*–73.
- (61) Xu, H.; Li, P. X.; Ma, K.; Thomas, R. K.; Penfold, J.; Lu, J. R. Limitations in the Application of the Gibbs Equation to Anionic Surfactants at the Air/Water Surface: Sodium Dodecylsulfate and Sodium Dodecylmonooxyethylenesulfate Above and Below the CMC. *Langmuir* **2013**, *29*, 9335–9351.
- (62) Wang, Z.; Li, P. X.; Ma, K.; Chen, Y.; Campana, M.; Penfold, J.; Thomas, R. K.; Roberts, D. W.; Xu, H.; Petkov, J. T.; et al. Impact of Molecular Structure, Headgroup and Alkyl Chain Geometry, on the Adsorption of the Anionic Ester Sulfonate Surfactants at the Air-Solution Interface, in the Presence and Absence of Electrolyte. *J. Colloid Interface Sci.* **2019**, *544*, 293–302.
- (63) Nguyen, T.; Nguyen, A. V. In Situ Investigation of Halide Co-Ion Effects on SDS Adsorption at Air-Water Interfaces. *Soft Matter* **2014**, 10, 6556–6563.

- (64) Winter, B.; Weber, R.; Hertel, I. V.; Faubel, M.; Vrbka, L.; Jungwirth, P. Effect of bromide on the interfacial structure of aqueous tetrabutylammonium iodide: Photoelectron spectroscopy and molecular dynamics simulations. *Chem. Phys. Lett.* **2005**, *410*, 222–227.
- (65) Zhao, T. T.; Xu, G. Y.; Yuan, S. L.; Chen, Y. J.; Yan, H. Molecular Dynamics Study of Alkyl Benzene Sulfonate at Air/Water Interface: Effect of Inorganic Salts. *J. Phys. Chem. B* **2010**, *114*, 5025–5033.
- (66) Uematsu, Y.; Bonthuis, D. J.; Netz, R. R. Charged Surface-Active Impurities at Nanomolar Concentration Induce Jones-Ray Effect. *J. Phys. Chem. Lett.* **2018**, *9*, 189–193.
- (67) Duignan, T. T.; Peng, M. S.; Nguyen, A. V.; Zhao, X. S.; Baer, M. D.; Mundy, C. J. Detecting the Undetectable: The Role of Trace Surfactant in the Jones-Ray Effect. *J. Chem. Phys.* **2018**, *149*, 194702.
- (68) Abranko-Rideg, N.; Darvas, M.; Horvai, G.; Jedlovszky, P. Immersion Depth of Surfactants at the Free Water Surface: A Computer Simulation and ITIM Analysis Study. *J. Phys. Chem. B* **2013**, *117*, 8733–8746.
- (69) The approximate 10 Å separation in depth profiles between sulfur and sodium has also been observed by Wang and Morgner for SDS in formamide. See ref 32.
- (70) Li, P. X.; Thomas, R. K.; Penfold, J. Limitations in the Use of Surface Tension and the Gibbs Equation To Determine Surface Excesses of Cationic Surfactants. *Langmuir* **2014**, *30*, 6739–6747.
- (71) Aleiner, G. S.; Us'yarov, O. G. Adsorption of Ions in the Dffuse Part of an Electrical Double Layer at Ionic Surfactant Solution-Air Interfaces in the Presence of Background Electrolytes. *Colloid J.* **2008**, 70, 263–267.
- (72) Shaloski, M. A.; Gord, J. R.; Staudt, S.; Quinn, S. L.; Bertram, T. H.; Nathanson, G. M. Reactions of  $\rm N_2O_5$  with Salty and Surfactant-Coated Glycerol: Interfacial Conversion of  $\rm Br^-$  to  $\rm Br_2$  Mediated by Alkylammonium Cations. *J. Phys. Chem. A* **2017**, *121*, 3708–3719.
- (73) Faust, J. A.; Dempsey, L. P.; Nathanson, G. M. Surfactant-Promoted Reactions of Cl<sub>2</sub> and Br<sub>2</sub> with Br<sup>-</sup> in Glycerol. *J. Phys. Chem. B* **2013**, *117*, 12602–12.
- (74) Brastad, S. M.; Albert, D. R.; Huang, M. W.; Nathanson, G. M. Collisions of DCl with a Solution Covered with Hydrophobic and Hydrophilic Ions: Tetrahexylammonium Bromide in Glycerol. *J. Phys. Chem. A* **2009**, *113*, 7422–7430.
- (75) Shaloski, M. A.; Sobyra, T. B.; Nathanson, G. M. DCI Transport through Dodecyl Sulfate Films on Salty Glycerol: Effects of Seawater Ions on Gas Entry. *J. Phys. Chem. A* **2015**, *119*, 12357–12366.